Chemical Engineering Journal 150 (2009) 213–222

Contents lists available at ScienceDirect

Chemical Engineering Journal

journal homepage: www.elsevier.com/locate/cej

A numerical study on premixed micro-combustion of CH_4–air mixture: Effects of combustor size, geometry and boundary conditions on flame temperature

J. Li[a], S.K. Chou[a,*], W.M. Yang[a], Z.W. Li[b]

[a] *Department of Mechanical Engineering, National University of Singapore, 9 Engineering Drive 1, Singapore 117576, Singapore*
[b] *SSLS, National University of Singapore, 5 Research Link, Singapore 117603, Singapore*

ARTICLE INFO

Article history:
Received 19 September 2008
Received in revised form 2 February 2009
Accepted 13 February 2009

Keywords:
Micro-combustion
Methane–air
Numerical simulation
Flame temperature
Boundary conditions

ABSTRACT

A numerical study on CH_4–air premixed combustion in micro-combustors was undertaken by solving the 2D governing equations. The effects of combustor size and geometry, inlet velocity profile and slip-wall boundary condition on the flame temperature were investigated. The simulation results showed that a larger combustor ($d = 2$ mm) gives higher flame temperature only when the flow velocity is below a certain level. With regard to the combustor geometry, a 2D planar channel ($H = 1$ mm) represents higher flame temperature than a cylindrical tube with $d = 2$ mm (equal hydrodynamic diameter), over the velocity range covered by the present study. In addition, it was noted that the flame temperatures in the cylindrical tube and 2D planar channel are quite close when $H = 0.65d$ is satisfied. The fully developed velocity profile applied at the inlet plane was found to have the flames anchored further from the entrance than the uniform profile, but no remarkable difference in terms of flame temperature (≤ 3 K) was observed. A simple analysis of the competing time scales (axial convection and radial diffusion) was presented to address the difference of flame structure between the methane–air and hydrogen–air mixtures. Finally, it was shown that in a combustor with $d = 1$ mm the effects of slip-wall boundary are negligible, compared to the bulk velocity and gases temperature.

1. Introduction

The demand for miniaturized power source is increasing with the proliferation of MEMS devices. Since Epstein and Senturia [1] proposed the concept of the 'micro-heat engine', a series of MEMS-based power generators have been prototyped, including the micro-gas turbine [2–4], the micro-thermoelectric device [5] and the micro-thermophotovoltaic (TPV) system [6,7]. Such work was mainly motivated by the fact that hydrogen and most hydrocarbon fuels represent much higher energy density than the most advanced lithium-ion batteries [8]. A key component of these various systems is a micro-combustor in which the fuel–air mixture is burned. The characteristic length of such micro-combustors may range from several millimeters down to the sub-millimeter scale. As a result of the reduced size of the combustors, combustion becomes less efficient due to the intensified heat loss from the flame to the combustor wall, radical destruction at the gas–wall interface and reduced residence time, making the system efficiency relatively low [9]. Despite the challenges ahead, the studies of 'micro-combustion engine' are still regarded as one of the promising frontiers of MEMS in the next 5–10 years [10].

For most hydrocarbon fuels, the quenching distance (also referred to as 'quenching diameter' for cylindrical tubes) is about a few millimeters, which is of the same order of magnitude of the flame thickness. For hydrogen, the flame can sustain in even smaller combustors. Previous experimental studies [11–13] demonstrated that self-sustained flames of CH_4–O_2 mixture can be achieved in a tube sized down to 0.5 mm in diameter. In the meanwhile, the numerical approach, which is able to yield detailed information of parameters within the small space, has been widely employed to study micro-combustion processes. Some numerical studies [14–20] and their major results are listed in Table 1. The simulation results of these studies revealed that (1) combustion (hydrogen and some hydrocarbon fuels) in micro-combustors sized down to the sub-millimeter scale is feasible, provided the heat losses are properly managed or the incoming unburned mixture is preheated; (2) heat recirculation through the wall via conduction is key in sustaining the flames in micro-combustors; (3) the dimensions (such as the length, gap/diameter, wall thickness and so on) of micro-combustors should be optimized in order to ensure efficient flames. By examining the effects of the key parameters such as

---

* Corresponding author.
E-mail address: mpecsk@nus.edu.sg (S.K. Chou).

1385-8947/$ – see front matter © 2009 Elsevier B.V. All rights reserved.
doi:10.1016/j.cej.2009.02.015

Nomenclature

A_k	pre-exponential factor of reaction rate (consistent unit)
c_p	specific heat (J/(kg K))
d	inner diameter (m)
d_m	molecule diameter (m)
D	diffusion coefficient (m^2/s)
D_i	diffusion coefficient of the ith species (m^2/s)
E_k	activation energy for the ith reaction (J/(kg mol))
h	enthalpy (J/kg)
h_{conv}	convective heat loss coefficient (non-insulated wall) (W/(m^2 K))
h_i	enthalpy of the ith species (J/kg)
h_{rad}	radiative heat loss coefficient (non-insulated wall) (W/(m^2 K))
H	spacing between the parallel plates (m)
k	thermal conductivity of gas (W/(m K))
k_B	Boltzmann constant (1.380662×10^{-23} J/K)
k_s	thermal conductivity of solid (W/(m K))
L	combustor length (m)
L_e	hydrodynamic entrance length (m)
$\hat{L}_e$	temperature-modified hydrodynamic entrance length (m)
m	mass of a molecule (kg)
$\dot{m}$	mass flow rate (kg/s)
p	pressure (Pa)
q	volumetric heat generation rate (W/m^3)
q_w	heat loss from the non-insulated wall (W)
r	radial coordinate (m)
r_0	inner radius (m)
R_u	universal gas constant (8314.41 J/(kg mol K))
R_0	outer radius (m)
t	wall thickness (m)
T	temperature (K)
$\bar{T}$	mean temperature (K)
T_0	ambient temperature (K)
T_f	flame temperature (K)
T_g	gases temperature at the interface (K)
T_s	temperature of solid (K)
T_u	temperature of unburned mixture (K)
T_w	wall temperature at the interface (K)
T_{wo}	temperature of the non-insulated wall (K)
u	axial velocity or x velocity (m/s)
u_0	incoming flow velocity (m/s)
u_g	axial velocity of the gases at the interface (m/s)
U_i	axial velocity or x velocity of the ith species (m/s)
u_w	axial velocity of the wall at the interface (m/s)
v	radial velocity or y velocity (m/s)
V_i	radial velocity or y velocity of the ith species (m/s)
x	axial coordinate or x coordinate (m)
y	y coordinate for 2D parallel plates (m)
Y_i	mass fraction of the ith species (kg/kg)

Greek symbols

β_k	temperature exponent of the ith reaction
γ	specific heat ratio
ρ	density of the mixture (kg/m^3)
ε	wall emissivity
λ	mean free path (m)
τ_C	time scale for axial conduction (s)
τ_D	time scale for radial diffusion (s)
Φ	fuel–air equivalence ratio
σ	Stefan–Boltzmann constant (5.67×10^{-8} W/(m^2 K^4))
σ_λ	momentum accommodation coefficient
σ_T	thermal accommodation coefficient
μ	dynamic viscosity (N s/m^2)
ω_i	production rate of the ith species (kmol/(m^3 s))

Dimensionless numbers

Kn	Knudsen number
Le	Lewis number
Pr	Prandtl number
Re	Reynolds number
Sc	Schmidt number

the flow rate, fuel–air equivalence ratio, wall thermal conductivity and heat losses from the non-insulated wall, these studies [14–19] were focused on the effects of design factors and operating conditions on the flame stability limits in micro-combustors. However, the flame structure inside micro-combustors was not given enough attention.

Flame temperature is one of the most important parameters to characterize a combustion process. In the context of micro-combustion, the understanding of flame temperature is necessary to choose the proper material for a micro-combustor. Besides silicon and some other semiconducting materials [2–4], high temperature materials such as SiC and Al_2O_3 have been used for the practical micro-combustors [10]. In this study, the effects of the combustor size and geometry, inlet velocity profiles and slip-wall boundary condition (at the gas–solid interface) on the flame temperature will be investigated. In view of the experimental work [12] that has developed a nearly ‘quench-less’ wall material which is resistant to radical quenching, the surface reactions occurring at the gas–solid interface are not included (same as Refs. [14,16–19]). Although our previous study [20] reported the simulation results of H_2–air premixed combustion in micro-combustors, the differences between hydrogen and methane as a result of fuel properties are quite significant to give rise to new observations, as can be seen in Table 2. Another reason for choosing methane as the fuel is that compared to those more complicated hydrocarbons, the detailed reaction mechanism has been well studied, allowing us to focus on the thermal issues without compromising the accuracy of kinetics.

2. Numerical model

Fig. 1 shows the cross-sectional view of the micro-channel (cylindrical tube and 2D parallel plates) in which steady-state combustion of a CH_4–air mixture takes place. The origin is fixed at the center of the inlet plane. x depicts the axial or downstream distance, and r or y represents the radial distance or distance from the centerline of the cylindrical tube or 2D parallel plates, respectively. An assumption is made that the swirl velocity component is zero, meaning a symmetrical flow with respect to the centerline. Thus, the case is simplified to a 2D problem. Only half of the combustor is considered to save the computational time. In addition, the following assumptions are made: (1) no Dufour effects [22]; (2) no gas radiation [16,17]; (3) no work done by pressure and viscous forces; (4) steady-state. With these assumptions, the governing equations of continuity, momentum, species and energy in the gas phase (for the cylindrical micro-combustor) can be written as follows:

Continuity

$$\frac{\partial(\rho u)}{\partial x} + \frac{1}{r}\frac{\partial(\rho v r)}{\partial r} = 0 \tag{1}$$

Table 1
Numerical studies on micro-combustion in simple geometries.

Authors	Fuel-oxidizer	Combustor geometry	Combustor size	Reaction mechanism	Major scope and focus
Raimondeau et al. [14]	CH_4 + air (Φ = 1.0)	Tubular micro-channel	Down to d = 200 μm	Detailed gas phase reactions	1. Discontinuity of temperature and species at the gas–solid interface; 2. Preheated fuel–air mixture.
Karagiannidis et al. [15]	CH_4 + air, fuel-lean	Plane channel	H = 1 mm, L = 10 mm	Detailed gas phase and surface reactions	1. Hetero/homogeneous combustion; 2. Elevated pressure up to 5 bar; 3. Limits of flame stability.
Norton and Vlachos [16]	C_3H_8 + air	Parallel plates	H = 600 μm, L = 10 mm	One-step global reaction	1. Flame stability in terms of extinction and blowout; 2. Parametric study.
Norton and Vlachos [17]	CH_4 + air (Φ = 1.0)	Parallel plates	H = 600 μm, L = 10 mm	One-step global reaction	1. Flame stability in terms of extinction and blowout; 2. Parametric study.
Hua et al. [18]	H_2 + air (Φ = 1.0)	Cylindrical chamber	Down to d = 0.1 mm	Detailed gas phase reactions	1. Expansion step as flame holder; 2. Adiabatic & non-adiabatic walls.
Kaisare and Vlachos [19]	CH_4 + air C_3H_8 + air (Φ = 1.0)	Parallel plates	H = 600 μm	One-step global reaction	1. Simplified 1-D reactor model; 2. Effects of fuel properties (CH_4 and C_3H_8); 3. Optimum reactor dimensions (gap, length, wall thickness, etc.).
Li et al. [20]	H_2 + air (Φ = 0.5)	Cylindrical tubes	d = 0.4–0.8 mm	Detailed gas phase reactions	1. Comparative study; 2. Effects of Knudsen number (velocity slip and temperature jump).

x momentum

$$\frac{\partial(\rho uu)}{\partial x} + \frac{1}{r}\ \frac{\partial(\rho uvr)}{\partial r} = -\frac{\partial p}{\partial x} + \frac{\partial}{\partial x}\left(\frac{4}{3}\mu\frac{\partial u}{\partial x}\right) + \frac{1}{r}\ \frac{\partial}{\partial r}\left(r\mu\frac{\partial u}{\partial r}\right) - \frac{\partial}{\partial x}\left(\frac{2\mu}{3r}\ \frac{\partial(vr)}{\partial r}\right) + \frac{1}{r}\ \frac{\partial}{\partial r}\left(r\mu\frac{\partial v}{\partial x}\right) \quad (2)$$

r momentum

$$\frac{\partial(\rho uv)}{\partial x} + \frac{1}{r}\frac{\partial(\rho vvr)}{\partial r} = -\frac{\partial p}{\partial r} + \frac{\partial}{\partial x}\left(\mu\frac{\partial u}{\partial r}\right) - \frac{1}{r}\frac{\partial}{\partial r}\left(\frac{2r\mu}{3}\frac{\partial u}{\partial x}\right) + \frac{\partial}{\partial x}\left(\mu\frac{\partial v}{\partial x}\right) + \frac{1}{r}\frac{\partial}{\partial r}\left(\frac{4r\mu}{3}\frac{\partial v}{\partial r}\right) - \frac{1}{r}\frac{\partial}{\partial r}\left(\frac{2}{3}\mu v\right) \quad (3)$$

Energy

$$\frac{\partial}{\partial x}(\rho uh) + \frac{1}{r}\frac{\partial}{\partial r}(\rho vhr) = \frac{\partial}{\partial x}\left(k\frac{\partial T}{\partial x}\right) + \frac{1}{r}\frac{\partial}{\partial r}\left(k\frac{\partial T}{\partial r}r\right) - \frac{1}{r}\frac{\partial}{\partial r}\left(r\rho\sum_{i=1}^{N}Y_i h_i V_i\right) - \frac{\partial}{\partial x}\left(\rho\sum_{i=1}^{N}Y_i h_i U_i\right) + q \quad (4)$$

Species conservation

$$\frac{\partial(\rho uY_i)}{\partial x} + \frac{1}{r}\frac{\partial(\rho vrY_i)}{\partial r} = \frac{\partial}{\partial x}\left[D_i\frac{\partial(\rho Y_i)}{\partial x}\right] + \frac{1}{r}\frac{\partial}{\partial r}\left[D_i r\frac{\partial(\rho Y_i)}{\partial r}\right] + \omega_i \quad (5)$$

The energy balance in the solid phase is given by

$$\frac{\partial}{\partial x}\left(k_s\frac{\partial T_s}{\partial x}\right) + \frac{1}{r}\frac{\partial}{\partial r}\left(k_s\frac{\partial T_s}{\partial r}r\right) = 0 \quad (6)$$

The skeletal mechanism (shown in Table 3) for methane oxidation (16 species and 25 reversible reactions) developed by Smooke and Giovangigli [23] is employed. The mechanism showed a good agreement between predicted and measured structures of one-dimensional macro-flames under a wide range of mixture compositions. In addition, its application in the simulation of micro-flames [24] was also found to be able to yield reasonable results. Compared to the one-step global reaction [17,19], the skeletal mechanism can better represent the reaction process as it involves partial oxidation, reverse reactions and intermediate products. Based on the above governing equations, the 2D fully elliptic simulations are performed such that heat and mass transfer in the gas phase as well as heat transfer in the solid phase are treated explicitly. The governing equations are discretized using the finite-volume method and solved by Fluent® Release 6.3 [25]. A first-order upwind scheme is used to discretize the governing equations and SIMPLE algorithm is used to deal with the pressure–velocity coupling. The

Table 2
Comparison of fuel properties between methane and hydrogen[a].

Properties	Methane	Hydrogen
High heating value (HHV)	55.5 MJ/kg	141.9 MJ/kg
Laminar flame speed (Φ = 1.0, p = 1 atm)	40 cm/s	210 cm/s
Adiabatic flame temperature (Φ = 1.0, p = 1 atm, with air)	2226 K	2400 K
Quenching distance (cold-wall, Φ = 1.0, p = 1 atm, with air)	2.5 mm	0.64 mm

[a] *Source*: data from Ref. [21].

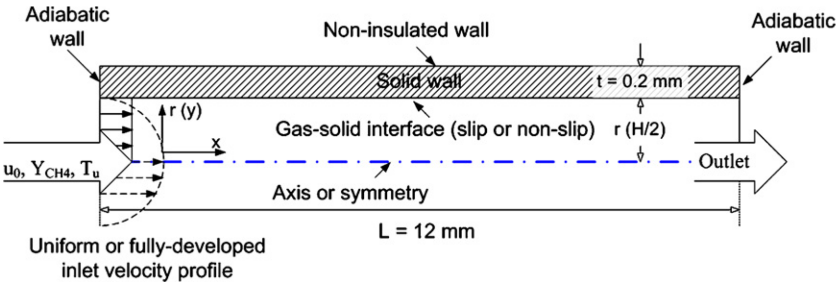

Fig. 1. Schematic of the computational domain with some boundary conditions (not to scale).

equations are solved implicitly with a 2D segregated solver using an under-relaxation method. The solver first solves the momentum equations, then the continuity equation, followed by the updating of the pressure and mass flow rates. The energy and species equations are subsequently solved. Iterations are monitored and checked until a converged solution is obtained. The convergence criteria for the scaled residuals are set to be 1×10^{-3} for continuity, 1×10^{-3} for velocity, 1×10^{-6} for energy and 1×10^{-3} for species concentration. The gas density is calculated using the ideal gas law. The gas viscosity, specific heat and thermal conductivity are calculated as a mass fraction-weighted average of all species. The specific heat of each species is calculated using a piecewise polynomial fit of temperature [26]. Numerical convergence is generally difficult because of the inherent stiffness of the matrix (chemistry) and the disparity between the wall and fluid thermal conductivities. For most cases, it was found that energy (temperature) is the last parameter to get converged. The larger number of elementary reactions and more participating species require more intensive computational power than the H_2–air combustion. Therefore, the simulations were executed using parallel computing on a cluster of PCs which have up to 16 GB of RAM. The CPU time for each case is about 10 h or longer (but less than 2 days), depending on the initial guess and the complexity of the case. The cases with the slip-wall condition normally take longer time to get converged.

Table 3

Skeletal mechanism for methane–air reaction[a].

Reactions	A_k (m, kmol, s)	β_k	E_k (J/kmol)
(1f) $H + O_2 \rightarrow OH + O$	2.000E+11	0.000	7.034E+07
(1b) $OH + O \rightarrow H + O_2$	1.575E+10	0.000	2.889E+06
(2f) $O + H_2 \rightarrow OH + H$	1.800E+07	1.000	3.695E+07
(2b) $OH + H \rightarrow O + H_2$	8.000E+06	1.000	2.830E+07
(3f) $H_2 + OH \rightarrow H_2O + H$	1.170E+06	1.300	1.518E+07
(3b) $H_2O + H \rightarrow H_2 + OH$	5.090E+06	1.300	7.782E+07
(4f) $OH + OH \rightarrow O + H_2O$	6.000E+05	1.300	0.000E+00
(4b) $O + H_2O \rightarrow OH + OH$	5.900E+06	1.300	7.130E+07
(5) $H + O_2 + M \rightarrow HO_2 + M$[b]	2.300E+12	-0.800	0.000E+00
(6) $H + HO_2 \rightarrow OH + OH$	1.500E+11	0.000	4.204E+06
(7) $H + HO_2 \rightarrow H_2 + O_2$	2.500E+10	0.000	2.931E+06
(8) $OH + HO_2 \rightarrow H_2O + O_2$	2.000E+10	0.000	4.187E+06
(9f) $CO + OH \rightarrow CO_2 + H$	1.510E+04	1.300	−3.174E+06
(9b) $CO_2 + H \rightarrow CO + OH$	1.570E+06	1.300	9.352E+07
(10f) $CH_4 + (M) \rightarrow CH_3 + H + (M)$[c]	6.300E+14	0.000	4.354E+08
(10b) $CH_3 + H + (M) \rightarrow CH_4 + (M)$[c]	5.200E+09	0.000	−5.485E+06
(11f) $CH_4 + H \rightarrow CH_3 + H_2$	2.200E+01	3.000	3.663E+07
(11b) $CH_3 + H_2 \rightarrow CH_4 + H$	9.570E−01	3.000	3.663E+07
(12f) $CH_4 + OH \rightarrow CH_3 + H_2O$	1.600E+03	2.100	1.030E+07
(12b) $CH_3 + H_2O \rightarrow CH_4 + OH$	3.020E+02	2.100	7.294E+07
(13) $CH_3 + O \rightarrow CH_2O + H$	6.800E+10	0.000	0.000E+00
(14) $CH_2O + H \rightarrow HCO + H_2$	2.500E+10	0.000	1.671E+07
(15) $CH_2O + OH \rightarrow HCO + H_2O$	3.000E+10	0.000	5.003E+06
(16) $HCO + H \rightarrow CO + H_2$	4.000E+10	0.000	0.000E+00
(17) $HCO + M \rightarrow CO + H + M$	1.600E+11	0.000	6.155E+07
(18) $CH_3 + O_2 \rightarrow CH_3O + O$	7.000E+09	0.000	1.074E+08
(19) $CH_3O + H \rightarrow CH_2O + H_2$	2.000E+10	0.000	0.000E+00
(20) $CH_3O + M \rightarrow CH_2O + H + M$	2.400E+10	0.000	1.206E+08
(21) $HO_2 + HO_2 \rightarrow H_2O_2 + O_2$	2.000E+09	0.000	0.000E+00
(22f) $H_2O_2 + M \rightarrow OH + OH + M$	1.300E+14	0.000	1.905E+08
(22b) $OH + OH + M \rightarrow H_2O_2 + M$	9.860E+08	0.000	−2.123E+07
(23f) $H_2O_2 + OH \rightarrow H_2O + HO_2$	1.000E+10	0.000	7.536E+06
(23b) $H_2O + HO_2 \rightarrow H_2O_2 + OH$	2.860E+10	0.000	1.373E+08
(24) $OH + H + M \rightarrow H_2O + M$[b]	2.200E+16	−2.000	0.000E+00
(25) $H + H + M \rightarrow H_2 + M$[b]	1.800E+12	−1.000	0.000E+00

[a] Rate constants are given in the form $k = A_k T^{\beta_k} \exp(-E_k/R_u T)$.

[b] Third body efficiencies: $CH_4 = 6.5$, $H_2O = 6.5$, $CO_2 = 1.5$, $H_2 = 1.0$, $CO = 0.75$, $O_2 = 0.4$ and $N_2 = 0.4$. All other species = 1.0.

[c] Lindemann form, $k = k_\infty/(1 + k_{fall}/[M])$ where $k_{fall} = 6.3 \exp(-7.536 \times 10^7/R_u T)$.

The wall thermal conductivity is taken to be 20 W/(m^2 K) (a typical value for stainless steel). The wall has a thickness of 0.2 mm and the combustor length is 12 mm. At the inlet plane, the mixture enters the combustor with a uniform temperature $T_u = 300$ K. Vlachos et al. [27] noted that for methane oxidation, the C1-path is the principal channel for fuel-lean flames, while the C2-path (conversion of CH_4 to higher hydrocarbons) which consists of about 200 elementary reactions becomes important for sufficiently fuel-rich mixtures. Therefore, the fuel–air equivalence ratio is chosen to be 0.9 to ensure that C1-path alone can give sufficient accuracy. At the combustor outlet, a far-field pressure condition is specified. Same as the cases for hydrogen combustion, the left and right sidewalls are assumed to be adiabatic (zero heat flux boundary condition) [16,17]. Heat losses from the non-insulated wall to the ambient are given by

$$q_w = h_{conv}(T_{wo} - T_0) + \varepsilon\sigma(T_{wo}^4 - T_0^4) \qquad (7)$$

where the convective heat transfer coefficient h_{conv} and the wall emissivity ε are taken to be 5 W/(m^2 K) (weak natural convection) and 0.2 (polished surface without serious oxidation), respectively.

In the gas phase, the mesh density was finalized to be 240 grids (an interval of 0.05 mm) and 25 grids (an interval of 0.02 mm) in the axial direction and radial direction, respectively. Higher grid densities were tested but no obvious advantage was found. A high temperature (~1600 K) is imposed on the entire computational domain (both gases and solid) as an initial guess for the numerical iteration. It is important to use a temperature high enough to 'ignite' the mixture. Lower temperature may fail ignition for some cases. The physical and boundary conditions summarized in this section are applied to all cases in this study. Other conditions may vary from case to case for the purpose of comparison and will be stated in the respective sections.

3. Results and discussion

3.1. Reference case

A 'reference case' needs to be defined in order to facilitate comparison. The geometry of the reference case is a cylindrical tube with an inner diameter of 1 mm. The boundary conditions are summarized as follows:

- *Inlet* ($x = 0$): $T_u = 300$ K, $u_0 = 0.3$, 0.5, 0.8 and 1.0 m/s, $Y_{CH_4} = 0.05$ (Y_{O_2} can be derived from $\Phi = 0.9$ and the air composition);
- *Centerline* ($r = 0$): $\partial u/\partial r = 0$, $\partial T/\partial r = 0$, $\partial Y_i/\partial r = 0$, $v = 0$ (no diffusion flux and zero convective flux across the symmetry plane);
- *Gas–solid interface* ($r = r_0$): $u = 0$, $v = 0$ (non-slip wall), $\partial Y_i/\partial r = 0$ (zero diffusion flux normal to the interface), and the heat flux at the interface is computed using Fourier's law and continuity in temperature and heat flux links the gas and solid phase;
- *Non-insulated wall* ($r = R_0$): $q_w = h_{conv}(T_{wo} - T_0) + \varepsilon\sigma(T_{wo}^4 - T_0^4)$.

Compared to the velocity range used for hydrogen ($u_0 = 1$–8 m/s) [20], much lower values are employed for methane, owing to its lower burning velocity (see Table 2). Based on the simulation results, it is noted that as the inlet velocity increases the flame is blown further downstream of the micro-combustor. Higher velocity which implies higher mass flow rate requires longer heating length (by the combustor wall) for the mixture to be heated up to ignition temperature. For $u_0 = 0.3$ m/s, the flame is anchored near the entrance and the highest temperature of gases lies at the centerline of the combustor. When the velocity increases to 0.5 m/s and above, the position of the highest temperature of gases shifts from the centerline to the wall. Fig. 2 shows the contours of temperature, methane mass fraction and axial velocity for the case of $u_0 = 0.5$ m/s. It can be seen that a major part of methane is consumed within a thin layer of reactions. Fig. 2 indicates that in the pre-flame zone, the wall temperature is higher than the mixture temperature, suggesting the direction of heat transfer is from the wall to the fuel–air mixture [16,17]. In contrast to the hydrogen–air mixture which has the high temperature zone attached to the combustor wall [20], the high temperature zone of the methane–air flames occupies a wider span of the radial section. The difference in terms of flame structure between methane and hydrogen is mainly attributed to the overall effects of the competing time scales for axial convection (flow velocity) and radial diffusion (mass diffusivity), which will be further elaborated in the following sections.

3.2. Combustor size and geometry

For the hydrogen–air mixture, it was shown that over the entire velocity span ($1 \le u_0 \le 8$ m/s) that was simulated—the smaller the combustor, the lower the flame temperature [20]. In order to investigate the effects of combustor size for the methane–air mixture, a larger combustor ($d = 2$ mm) is modeled. Other conditions (wall thickness, combustor length, boundary conditions, etc.) are identical to those for the reference case ($d = 1$ mm). By defining the flame temperature as the highest temperature in the gas phase, the effects of combustor size on the flame temperature are shown in Fig. 3. Lines connecting symbols are only for the sake of visualization. For both combustors, the increase of inlet velocity results in higher flame temperature. However, when the inlet velocity is higher than 0.5 m/s, the smaller combustor ($d = 1$ mm) gives higher flame temperature than the larger one ($d = 2$ mm). In order to understand this result, the flame structure needs to be examined. For the $d = 2$ mm combustor, the flame shows a similar pattern to that of the hydrogen–air mixture, that is, the high temperature zone is attached to the combustor wall. The temperature contours for the $d = 2$ mm micro-combustor with medium ($u_0 = 0.5$ m/s) and high ($u_0 = 1.0$ m/s) velocities are shown in Fig. 4(a). Compared to Fig. 2 ($d = 1$ mm), the difference in terms of flame structure is obvious. As the combustor diameter is increased from 1 to 2 mm, the radial length for mass diffusion is doubled. As a result, the temperature at the centerline zone of the larger combustor is more controlled by axial convection than radial diffusion. Since the high temperature zone is shifted to the wall, heat diffuses in the radial direction to the centerline zone, which contributes to the lowered flame temperature. In addition, another factor that needs to be considered is that heat recirculation through the combustor wall is more significant in the smaller micro-combustor. Norton and Vlachos [17] obtained super-adiabatic flame temperature for the methane–air mixture in the micro-channels, which was attributed to the preheating of the

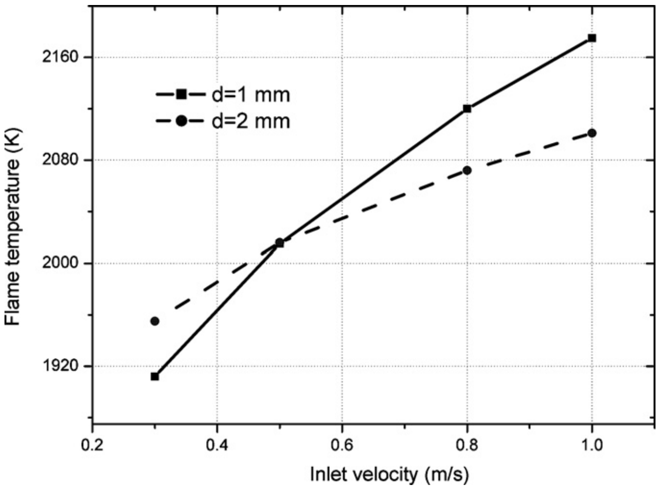

Fig. 3. Effects of combustor size on the flame temperature, cylindrical tube.

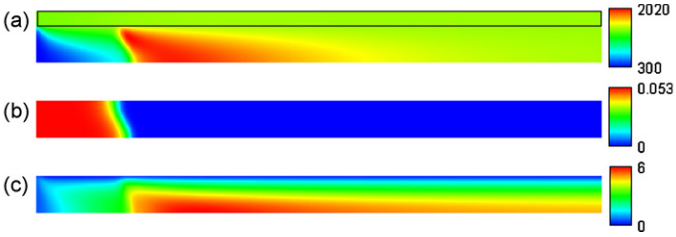

Fig. 2. Contours of (a) temperature, (b) methane mass fraction and (c) axial velocity, $d = 1$ mm, $u_0 = 0.5$ m/s, (a) for both solid and gas phase, (b) and (c) for gas phase only.

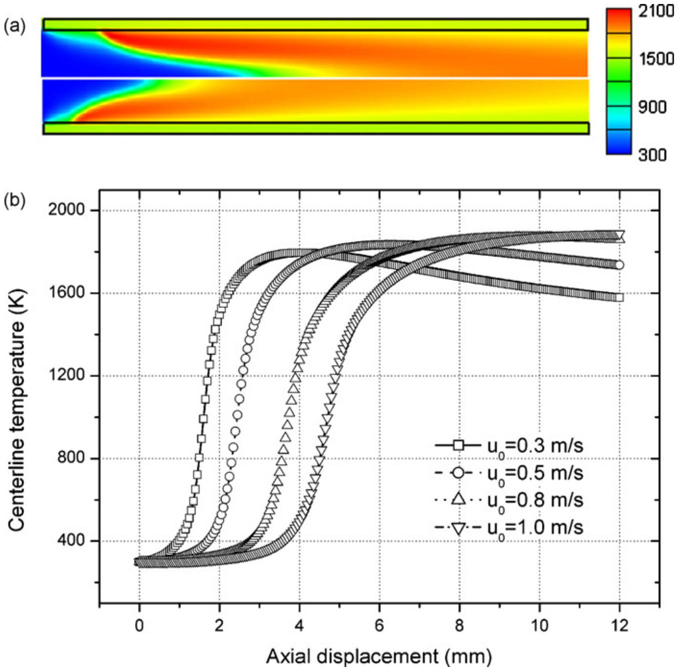

Fig. 4. Results of the cylindrical combustor with $d = 2$ mm: (a) temperature contours, $u_0 = 0.5$ m/s (lower) and $u_0 = 1.0$ m/s, unit in K and (b) centerline temperature profiles.

unburned mixture by heat recirculation through the wall. Apart from the explanations given above, incomplete combustion could also be a possible reason for the lowered flame temperature in the larger combustor ($d = 2$ mm). Fig. 4(b) shows the centerline temperature profiles for different flow velocities. It can be seen that as the velocity is increased to 0.8 m/s, the highest centerline temperature occurs close to or at the combustor exit, implying that the combustion process could be incomplete. Based on the limited cases simulated in the present study, it is noted that for CH_4–air premixed combustion, when the flow velocity is above a certain level, the conclusion that ‘smaller combustor gives lower flame temperature’ does not hold.

The geometry is another important factor for combustor design. Cylindrical tubes and rectangular channels are the two commonly used geometries. For simplicity, a model of 2D parallel plates is employed to represent the rectangular channels. In the simulation, the spacing (H) between the plates is taken to be 1 mm, same as the inner diameter in the reference case. Thus, the hydrodynamic diameter (=2H) of the 2D case is twice that of the cylindrical tube ($d = 1$ mm). Other physical and boundary conditions remain unchanged from the reference case. A theoretical analysis [28] showed that the quenching distance for the parallel plates is related to that for the cylindrical tube by a factor of 0.65. In other words, when $H = 0.65\,d$, the heat loss condition of a cylindrical tube is identical to a 2D planar channel. Therefore, one more 2D case with the spacing of $H = 0.65 \times 1 = 0.65$ mm is modeled for comparison. The variation of flame temperature with the flow velocity for the three cases is plotted in Fig. 5. Lines connecting symbols are only for the sake of visualization. The cylindrical tube with $d = 2$ mm is not included to avoid repetition, but it will be discussed in comparison with the 2D case with $H = 1$ mm. From Fig. 5, it can be seen that the $H = 1$ mm case has higher flame temperature than the $d = 1$ mm case over the entire velocity range, owing to the difference in the hydrodynamic diameter. However, in contrast to the cylindrical tube with $d = 2$ mm (shown in Fig. 3) which has the same hydrodynamic diameter, the 2D channel with $H = 1$ mm also gives higher flame temperature. Other than the factors (radial diffusion, heat recirculation and incomplete combustion) discussed above, the difference in terms of heat loss area between the two geometries could be another reason. More in-depth investigation on this result is needed, but it can be concluded at this point that the hydrodynamic diameter alone is not sufficient to correlate the two combustor geometries. For the 2D case with $H = 0.65$ mm, it is shown that both the trend and the value of the flame temperature are very similar to the cylindrical tube with $d = 1$ mm, with the maximum temperature difference about 25 K at $u_0 = 0.3$ m/s. The above result indicates that the factor of 0.65 is a fairly good estimate, based on the limited cases simulated in this study. Together with the result for the hydrogen–air mixture [20], it is concluded that the factor of 0.65 is applicable to both hydrogen–air and methane–air mixtures in micro-combustors sized up to 1 mm in diameter. This conclusion could be useful when attempting to alter the shape of the micro-combustor without affecting the flame temperature too much. However, it should be noted that in practice, the result may not be strictly valid due to the three-dimensional nature of a rectangular planar channel.

3.3. Inlet velocity profile

The two types of inlet velocity profile commonly specified for numerical simulation are uniform and fully developed (FD for short) velocity profiles. In practice, the uniform velocity profile may be obtained by directing the flow through some porous media, while the FD velocity profile may be realized by using a long connection tube in order for the flow to get fully developed before entering the combustor. For the FD velocity profile, the axial velocity at the inlet plane is given by

$$u(r) = 2u_0\left[1 - \left(\frac{r}{r_0}\right)^2\right] \qquad (8)$$

where u_0 is velocity for the uniform case. Eq. (8) ensures the same mass flow rate at the inlet plane. Other boundary conditions remain unchanged from the reference case. The temperature contours obtained by using the two velocity profiles are plotted in Fig. 6. No significant difference ($\leq$3 K) in terms of flame temperature is found over the entire velocity span. However, it can be seen that the inlet velocity profile affects the position where the flame is anchored. It is clearly shown that the FD profile stabilizes the flame further from the entrance than the uniform profile does, and the difference increases with the increasing velocity. The flame position is essentially an overall result of the thermal conditions and the flow field. In the pre-flame zone, the inlet velocity profile may affect the heat transfer from the wall to the unburned mixture, thus affecting the heating length for the ignition to occur. On the other hand, flame stabilization is achieved in the velocity boundary layer in which the flame speed (burning velocity) reaches an equilibrium with the flow velocity. It is hard to predict the flame position due to the close coupling between the thermal (both gases and solid) and flow fields in the micro-combustors. Therefore, it should be pointed

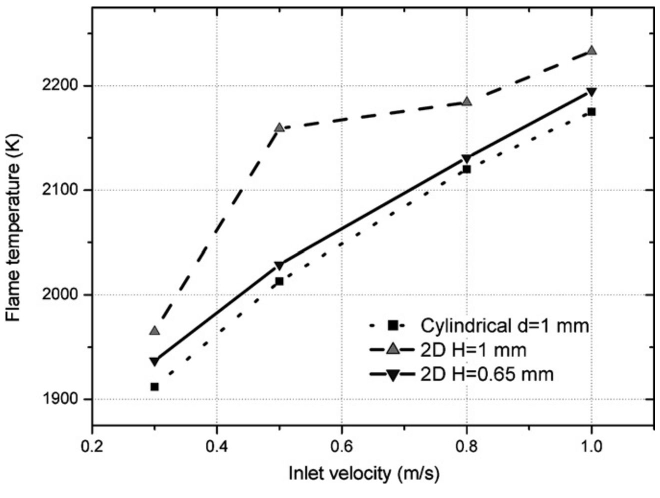

Fig. 5. Effects of combustor geometry on the flame temperature.

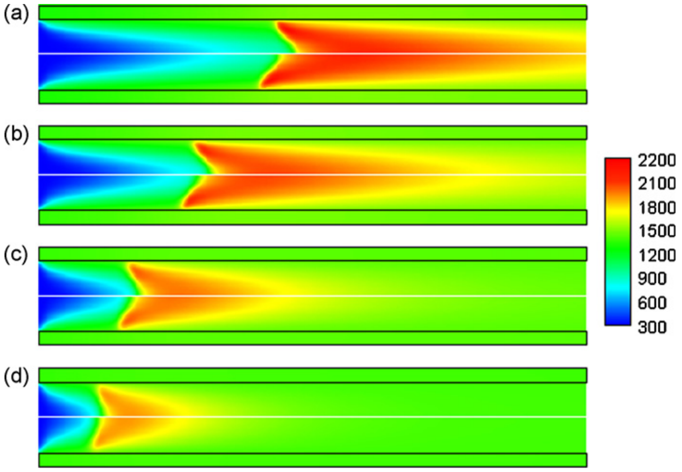

Fig. 6. Temperature contours (unit: K), upper half for FD and lower for uniform, $d = 1$ mm, (a) $u_0 = 1.0$, (b) $u_0 = 0.8$, (c) $u_0 = 0.5$ and (d) $u_0 = 0.3$ m/s.

out that the conclusion made above regarding the flame position is only valid for the particular cases shown in Fig. 6.

The flows with chemical reactions are far more complicated than non-reacting flows. For a flow to be fully developed, there are twofold meaning: hydrodynamic and thermal. A hydrodynamic FD flow requires the radial velocity profile approaches Hagen-Poiseuille profile, while a thermally FD flow requires attaining a radially uniform temperature distribution. Due to the reactions taking place along the flowing path, it is expected that these two criteria are not met at the same axial position. For the non-reacting flows, the hydrodynamic entrance length is given by [29]

$$L_e = 0.05 Re \cdot d = 0.05 \frac{\rho u d^2}{\mu} \tag{9}$$

According to mass conservation, one has

$$(\rho u)\pi r_0^2 = \dot{m} = \text{constant} \tag{10}$$

At a result of heat generation, the gases temperature experiences significant change while flowing through the micro-combustor, giving rise to the change of the mixture properties. Thus, it is necessary to modify the Reynolds number which is evaluated at the inlet plane. The kinetic theory of transport properties gives [29]:

$$\mu = \frac{5}{16} \cdot \frac{\sqrt{\pi m k_B T}}{\pi {d_m}^2} \tag{11}$$

which shows that μ is proportional to $T^{1/2}$. Therefore, the temperature-modified hydrodynamic entrance length can be written as follows

$$\hat{L}_e = 0.05\,\widehat{Re} \cdot d = 0.05\, Re_0 \cdot \sqrt{\frac{T_u}{\overline{T}}} \cdot d \tag{12}$$

where $\overline{T} = (T_u + T_f)/2$ is the mean temperature and Re_0 refers to the Reynolds number evaluated based on the fluid properties at the inlet plane. Fig. 7 shows the calculated hydrodynamic entrance lengths and the positions of the highest centerline temperature and the highest averaged temperature over the radial direction. It can be seen from Fig. 7 that as the velocity increases, the difference between the FD and uniform cases becomes larger. In contrast to the hydrogen–air mixture [20] that the position of the highest centerline temperature nearly coincides with the temperature-modified hydrodynamic entrance length given by Eq. (12), the methane–air mixture takes much longer distance to reach its peak centerline temperature. In addition to the significant difference in terms of chemical kinetics, mass diffusivity is playing an important role in yielding this result. The high mass diffusivity of hydrogen ($Le \approx 0.3$) results in the combustion zone concentrated close to the wall where flow velocity is relatively lower than the centerline zone. The heat then diffuses radially to the centerline region such that the position of the highest centerline temperature is mainly determined by aerodynamics (entrance length). For the methane–air mixture, much lower flow velocity was used than the hydrogen–air counterpart. As a result, although methane ($Le \approx 1.0$) has lower mass diffusivity than hydrogen, the relative importance of diffusion (in the radial direction) is comparable to convection (in the axial direction) such that the flame can reach the centerline over the radial direction and the position of the highest centerline temperature is primarily dependent on chemical kinetics. In order to understand the relative significance of axial convection and radial diffusion, a simple analysis is done to examine the characteristic time scales for the two competing factors. For a combustion flow in a cylindrical micro-combustor, the time scale of axial convection can be represented as $\tau_C \sim L/u_0$, and the time scale for radial diffusion is given by $\tau_D \sim r_0^2/D$. Thus, the ratio of the two time scales is

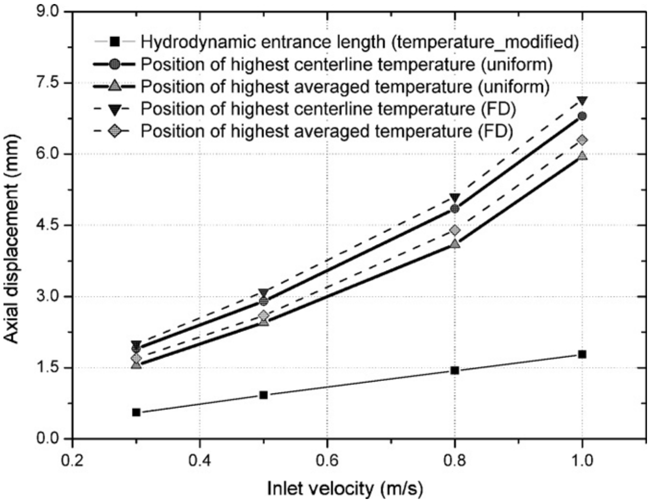

Fig. 7. Calculated hydrodynamic entrance lengths and the simulation results of the positions of the highest temperature, $d = 1$ mm.

$$\frac{\tau_C}{\tau_D} \sim \frac{L}{u_0}\frac{D}{r_0^2} = \frac{2L}{r_0}\frac{D}{\nu}\frac{\nu}{2r_0u_0} = \frac{2L}{r_0}\frac{1}{Sc\, Re_0} \tag{13}$$

where Re_0 is the Reynolds number evaluated based on the conditions at the combustion inlet. For the two mixtures that have been investigated (the current methane–air and hydrogen–air in a cylindrical tube with $d = 0.8$ mm and $L = 8$ mm [20]), it gives

$$\frac{(\tau_C/\tau_D)_{CH_4}}{(\tau_C/\tau_D)_{H_2}} = \frac{L_{CH_4}}{L_{H_2}}\frac{r_{0,H_2}}{r_{0,CH_4}}\frac{Sc_{H_2}}{Sc_{CH_4}}\frac{Re_{0,H_2}}{Re_{0,CH_4}} = \frac{12}{8}\frac{0.4}{0.5}\frac{0.2}{0.7}\frac{Re_{0,H_2}}{Re_{0,CH_4}}$$
$$= 0.34\frac{Re_{0,H_2}}{Re_{0,CH_4}} \tag{14}$$

where the values for the Schmidt numbers are taken from Ref. [30]. To have a similar flame structure to the methane–air mixture (i.e. occupying a wide span of the radial section, as shown in Fig. 6), the ratio given by Eq. (14) should be less than unity. Using $u_0 = 0.8$ m/s ($u_0 = 1.0$ m/s has the flame stretched to the combustion exit, which is prone to incomplete combustion) to quantify the Reynolds number for methane, the critical inlet velocity for the hydrogen–air mixture is about 2.9 m/s—the maximum u_0 that allows the flame to have a similar structure to the methane–air mixture shown in Fig. 6. Referring back to Ref. [20], it was shown that when $u_0 = 2$ m/s the hydrogen–air flame was already attached to the wall, indicating that the above analysis overestimates the upper limit of the inlet velocity. However, in view of the simplicity of the above analysis, Eq. (13) is still useful in giving qualitatively sound result.

The normalized velocity and temperature profiles in the radial direction for the case of $u_0 = 0.5$ m/s are plotted in Fig. 8. It can be seen that the difference in terms of radial velocity distribution caused by the inlet velocity profile prevails only at the near-entrance zone. Fig. 8 suggests that at an axial distance of around 1.5 mm from the entrance, a hydrodynamic FD velocity profile is almost formed for both cases. However, according to Fig. 8, the temperature profiles indicate that up to a distance of 1.5 mm the flow is simply being heated up without noticeable heat release. When the mixture flows further downstream (a distance of about 2 mm from the entrance), some exothermic reactions are initiated, indicated by the high temperature zone being shifted from the wall boundary to the centerline. From that position onwards, more reactions are being triggered along the flowing path, with both the flow and temperature fields being restructured.

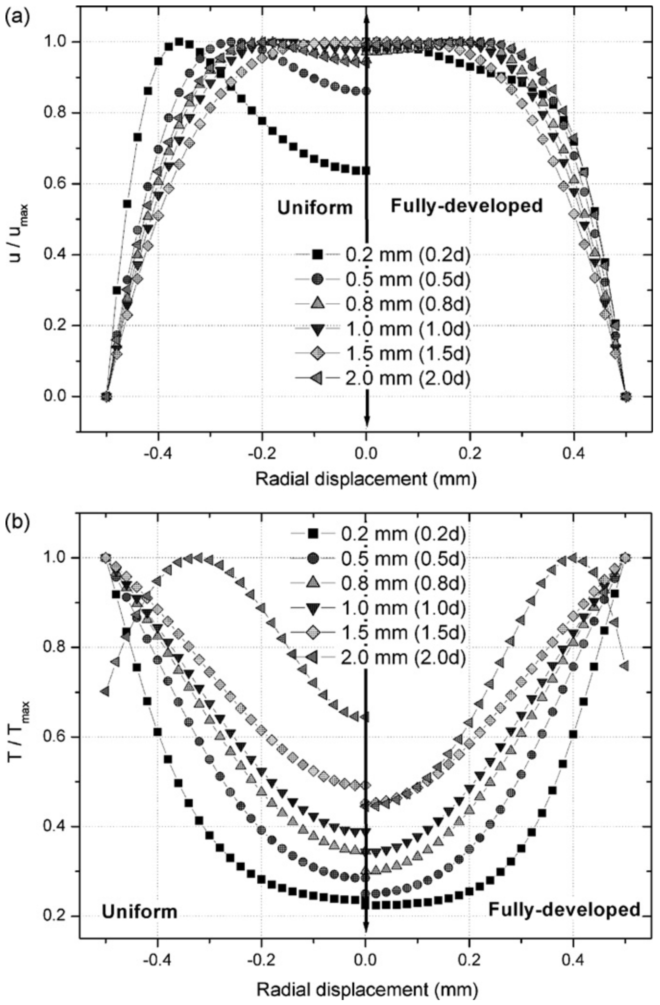

Fig. 8. Normalized axial velocity and temperature profiles, $d = 1$ mm, $u_0 = 0.5$ m/s: (a) axial velocity and (b) temperature.

3.4. *Slip-wall boundary condition*

Different from the parameters studied in the above sections which could be realized physically, the slip-wall boundary condition is a result of the reduced dimension. The purpose of this study is to examine the effects of velocity slip and temperature jump at the gas–solid interface on the temperature and flow field in micro-combustors. Slip-wall condition has been employed in studying the heat transfer problems in the micro-channels [31–33]. Raimondeau et al. [14] included the temperature jump at the interface in simulating the combustion flows in the micro-tubes, but the velocity slip was not considered in their study. In the micro-channel flows, the Knudsen number reflects the degree of rarefaction. For the Knudsen number in the range $10^{-3} \leq Kn \leq 10^{-1}$, a slip flow may be assumed. Taking the mean free path of air at the standard condition to be 0.1 μm, the Knudsen number for the reference case ($d = 1$ mm) is 1×10^{-4}, which is out of the slip flow regime. However, it should be noted that the mean free path is proportional to the temperature, as can be seen in Eq. (17) which is shown below. In a combustion process, there is a sharp temperature increase in the flame zone due to the release of chemical energy, leading to the increase of free mean path of the gases. Based on the simulation cases in this study, the flame temperature can reach about 2000 K. According to Eq. (17), the free mean path will be around seven times that of the initial state ($T_u = 300$ K), giving the Knudsen number to be 7×10^{-4}, which is very close to the lower limit of the slip flow regime. Although still not fully justified, the complete slip-wall condition is employed since the purpose of this investigation is to evaluate its effects on the temperature and flow field. The complete velocity slip and temperature jump at the interface are given by [32]:

$$u_s - u_w = \frac{2-\sigma_\lambda}{\sigma_\lambda}\lambda\left(\frac{\partial u}{\partial r}\right)_w + \frac{3}{4}\frac{\mu}{\rho T}\left(\frac{\partial T}{\partial r}\right)_w \tag{15}$$

$$T_s - T_w = \frac{2-\sigma_T}{\sigma_T}\left(\frac{2\gamma}{\gamma+1}\right)\frac{\lambda}{Pr}\left(\frac{\partial T}{\partial r}\right)_w \tag{16}$$

where σ_λ and σ_T are the momentum and thermal accommodation coefficients, respectively. For a given gas, their values depend on the surface finish and the fluid temperature and pressure, and are normally determined experimentally. In the present study, they are both taken to be unity [33]. λ is the mean free path given by [29]:

$$\lambda = \frac{k_B T}{\sqrt{2}\pi d_m^2 p} \tag{17}$$

For simplicity, an average value of the molecular diameters, $d_m = 3.65 \times 10^{-10}$ m, is used. γ and Pr are taken to be 1.4 and 0.7 (typical values for air), respectively. The second term on the right-hand side of Eq. (15) is one order of magnitude of Kn less than the first term [32], therefore is ignored in the simulation. Based on the above information, the user-defined function (UDF) incorporating the slip-wall condition is written as a subroutine and solved by Fluent® Release 6.3 [25]. This boundary condition is applied throughout the gas phase despite that the Knudsen number in some region might be even lower than 7×10^{-4} due to the lower gas temperature.

Over the span of the inlet velocity ($u_0 = 0.3$–1.0 m/s), no remarkable difference (the slip-wall condition gives 1–2 K higher) in terms of flame temperature is observed between the non-slip and slip-wall conditions. Some insight into this finding can be obtained through a simple inspection of the mathematical formulation of the slip-wall boundary condition. For the case of non-slip wall ($T_w = T_s$), the temperature gradient at the interface is given by

$$\left(\frac{\partial T}{\partial r}\right)_w = \frac{T_w - T_c}{\Delta r} \tag{18}$$

where T_c is the temperature of gases in the cell next to the interface. With the slip-wall boundary condition applied ($T_w \neq T_s$), in the region where the wall heats up the gases (pre-flame zone), there is $(\partial T/\partial r)_w > 0$ and Eq. (16) leads to $T_w > T_s$. Then one has

$$0 < \left(\frac{\partial T}{\partial r}\right)'_w = \frac{T_s - T_c}{\Delta r} < \frac{T_w - T_c}{\Delta r} = \left(\frac{\partial T}{\partial r}\right)_w \tag{19}$$

where $(\partial T/\partial r)'_w$ refers to the 'new' temperature gradient as a result of the slip-wall boundary condition. Eq. (19) simply implies less heat gained from the hotter wall to preheat the unburned mixture, which may result in longer heating length. Similarly, in the region where the gases are hotter than the wall (flame and post-flame zone), there is $(\partial T/\partial r)_w < 0$ and $T_s > T_w$. Therefore, one obtains

$$0 > \left(\frac{\partial T}{\partial r}\right)'_w = \frac{T_s - T_c}{\Delta r} > \frac{T_w - T_c}{\Delta r} = \left(\frac{\partial T}{\partial r}\right)_w \tag{20}$$

which leads to $|(\partial T/\partial r)'_w| < |(\partial T/\partial r)_w|$. This means that the heat conduction from the hotter gases to the wall is reduced. To summarize, the implementation of slip-wall boundary condition reduces the heat transfer between the gases and wall across the interface. As a result, there will be longer heating length for the mixture to reach the ignition state and higher flame temperature due to the reduced heat loss to the wall in the flame zone.

From Eqs. (15) and (16), it can be seen that the magnitude of temperature jump and velocity slip is closely related to the temperature

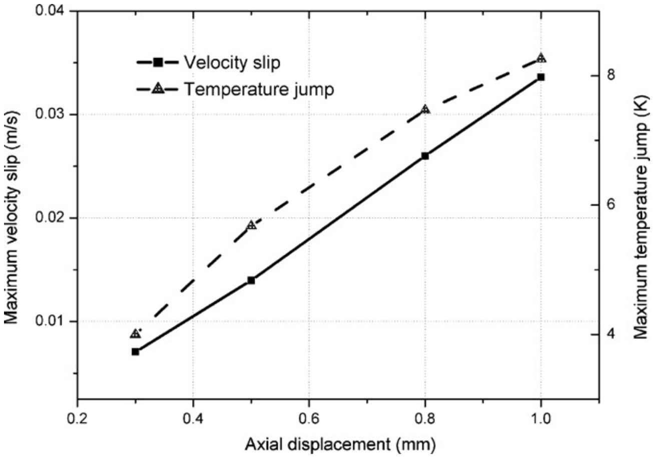

Fig. 9. Magnitude of maximum velocity slip and temperature jump, $d = 1$ mm.

and velocity gradients at the interface. Fig. 9 shows the maximum temperature jump and velocity slip against the inlet velocity. It can be seen that both of them increase with the increasing velocity. The maximum temperature jump occurs at the flame region where sharp temperature gradient (both radial and axial) exists. The velocity slip and temperature jump, compared to the bulk flow velocity and temperature, are practically negligible. Therefore, it is safe to conclude that for the methane–air mixture, the effects of the slip-wall boundary condition can be ignored, provided the inner diameter of the micro-combustor is not smaller than 1 mm.

4. Conclusion

Flame temperature is one of the most important parameters to characterize a combustion process. In the context of micro-combustion, the understanding of flame temperature is important to choose the proper materials for micro-combustors. A numerical study of CH_4–air premixed combustion in micro-combustors was undertaken by examining the effects of combustor size and geometry, inlet velocity profiles and slip-wall boundary condition on the flame temperature. A reference case was defined as a premixed methane–air combustion in a cylindrical tube ($d = 1$ mm and $L = 12$ mm) with a non-slip wall and a uniform velocity profile at the inlet plane. The flame structure of the methane–air mixture is essentially different from the hydrogen–air counterpart due to the great difference of fuel properties. It was shown that a larger combustor ($d = 2$ mm) gives higher flame temperature only when the flow velocity is below a certain level. With regard to the combustor geometry, a 2D planar channel ($H = 1$ mm) represents higher flame temperature than a cylindrical tube with $d = 2$ mm (equal hydrodynamic diameter), over the entire range of the inlet velocity investigated in the present study. Based on the limited cases simulated, it was noted that the flame temperatures in the cylindrical tube and 2D planar channel are quite close when $H = 0.65d$ is satisfied. Two types of velocity profile were applied at the inlet plane, and no remarkable difference (≤ 3 K) in terms of flame temperature was found. However, the flames were found to be stabilized further from the entrance when the FD velocity profile is employed. In order to understand the flame structure, a simple analysis of the competing time scales (axial convection and radial diffusion) was presented to address the difference between the methane–air and hydrogen–air mixtures. Finally, the slip-wall (velocity slip and temperature jump) boundary condition was applied at the gas–solid interface of the reference case ($d = 1$ mm). The inclusion of the slip-wall condition slightly increased the flame temperature by less than 2 K. However, compared to the bulk velocity and temperature of the reacting gases, the velocity slip and temperature jump were found to be negligible.

Acknowledgements

The authors would like to thank the Computer Center, National University of Singapore (NUS), for providing the software Fluent® and the supercomputing workstations. In addition, the authors are grateful to Mr. Wang Junhong of the NUS Computer Center, for his technical support and assistance in applying parallel computing in Fluent®.

References

[1] A.H. Epstein, S.D. Senturia, Macro power from micro machinery, Science 276 (1997) 1211.

[2] A. Mehra, A.A. Ayón, I.A. Waitz, M.A. Schmidt, Microfabrication of high-temperature silicon devices using wafer bonding and deep reactive ion etching, J. MEMS 8 (1999) 152–160.

[3] J.S. Hua, M. Wu, K. Kumar, Numerical simulation of the combustion of hydrogen–air mixture in micro-scaled chambers. Part II. CFD analysis for a micro-combustor, Chem. Eng. Sci. 60 (2005) 3507–3515.

[4] X.C. Shan, Z.F. Wang, Y.F. Jin, M. Wu, J. Hua, C.K. Wong, R. Maeda, Studies on a micro combustor for gas turbine engines, J. Micromech. Microeng. 15 (2005) S215–221.

[5] L. Sitzki, K. Borer, E. Schuster, P.D. Ronney, S. Wussow, Combustion in microscale heat-recirculating burners, in: Proceedings of The Third Asia-Pacific Conference on Combustion, Seoul, Korea, 2001.

[6] W.M. Yang, S.K. Chou, C. Shu, Z.W. Li, H. Xue, Development of microthermophotovoltaic system, Appl. Phys. Lett. 81 (2002) 5255–5257.

[7] W.M. Yang, S.K. Chou, C. Shu, H. Xue, Z.W. Li, Development of a prototype micro-thermophotovoltaic power generator, J. Phys. D: Appl. Phys. 37 (2004) 1017–1020.

[8] P.D. Ronney, Analysis of non-adiabatic heat-recirculating combustors, Combust. Flame 135 (2003) 421–439.

[9] A.C. Fernandez-Pello, Micropower generation using combustion: issues and approaches, Proc. Combust. Inst. 29 (2002) 883–898.

[10] W.H. Ko, Trends and frontiers of MEMS, Sens. Actuators A 136 (2007) 62–67.

[11] B.P. Mellish, F.J. Miller, J.S. Ti'en, D.L. Dietrich, P.M. Struk, Premixed flames stabilized on or propagating inside microtubes, in: The Fourth Joint Meeting U.S. Sections Combust. Inst, Philadelphia, PA, 2005.

[12] C.M. Miesse, R.I. Masel, C.D. Jensen, M.A. Shannon, M. Short, Submillimeter-scale combustion, AIChE J. 50 (2004) 3206–3214.

[13] G.A. Boyarko, C. Sung, S.J. Schneider, Catalyzed combustion of hydrogen–oxygen in platinum tubes for micro-propulsion applications, Proc. Combust. Inst. 30 (2005) 2481–2488.

[14] S. Raimondeau, D. Norton, D.G. Vlachos, R.I. Masel, Modeling of high-temperature microburners, Proc. Combust. Inst. 29 (2002) 901–907.

[15] S. Karagiannidis, J. Mantzaras, G. Jackson, K. Boulouchos, Hetero-/homogeneous combustion and stability maps in methane-fueled catalytic microreactors, Proc. Combust. Inst. 31 (2007) 3309–3317.

[16] D.G. Norton, D.G. Vlachos, A CFD study of propane/air microflame stability, Combust. Flame 138 (2004) 97–107.

[17] D.G. Norton, D.G. Vlachos, Combustion characteristics and flame stability at the microscale: a CFD study of premixed methane/air mixtures, Chem. Eng. Sci. 58 (2003) 4871–4882.

[18] J.S. Hua, M. Wu, K. Kumar, Numerical simulation of the combustion of hydrogen–air mixture in micro-scaled chambers. Part I. Fundamental study, Chem. Eng. Sci. 60 (2005) 3497–3506.

[19] N.S. Kaisare, D.G. Vlachos, Optimal reactor dimensions for homogeneous combustion in small channels, Catal. Today 120 (2007) 96–106.

[20] J. Li, S.K. Chou, Z.W. Li, W.M. Yang, A comparative study of H_2–air premixed flame in micro combustors with different physical and boundary conditions, Combust. Theory Model. 12 (2008) 325–347.

[21] S.R. Turns, An introduction to Combustion: Concepts and Applications, McGraw-Hill, New York, 2000.

[22] F.A. Williams, Combustion Theory: Fundamental Theory of Chemical Reacting Flow Systems, Benjamin/Cummings, Menlo Park, 1985.

[23] M.D. Smooke, V. Giovangigli, in: M.D. Smooke (Ed.), Formulation of the Premixed and Nonpremixed Test Problems in Reduced Kinetic Mechanisms and Asymptotic Approximations for Methane–Air Flames, Springer-Verlag, Berlin, 1991, pp. 1–28.

[24] K.H. Lee, O.C. Kwon, A numerical study on structure of premixed methane–air microflames for micropower generation, Chem. Eng. Sci. 62 (2007) 3710–3719.

[25] Fluent Inc., Fluent Release 6. 3 User Guide, Fluent Inc., 2006.

[26] R.J. Kee, R.M. Rupley, J.A. Miller, The CHEMKIN thermodynamic database, Sandia National Laboratories, 1992, Report No. SAND87-8215B.

[27] D.G. Vlachos, L.D. Schmidt, R. Aris, Ignition and extinction of flames near surfaces: Combustion of CH_4 in air, AIChE J. 40 (1994) 1005–1017.

[28] R.A. Strehlow, Combustion Fundamentals, McGraw-Hill, New York, 1984.

[29] R.J. Kee, M.E. Coltrin, P. Glarborg, Chemically Reacting Flow: Theory and Practice, John Wiley & Sons, NJ, 2003.

[30] R.-H. Chen, A. Kothawala, M. Chaos, L.P. Chew, Schmidt number effects on laminar jet diffusion flame liftoff, Combust. Flame 141 (2005) 469–472.
[31] R.F. Barron, X. Wang, T.A. Ameel, R.O. Warrington, The Graetz problem extended to slip-flow, Int. J. Heat Mass Transfer 40 (1997) 1817–1823.
[32] D. Jie, X. Diao, K.B. Cheong, L.K. Yong, Navier-Stokes simulations of gas flow in micro devices, J. Micromech. Microeng. 10 (2000) 372–379.
[33] M. Renksizbulut, H. Niazmand, G. Tercan, Slip-flow and heat transfer in rectangular microchannels with constant wall temperature, Intl. J. Thermal Sci. 45 (2006) 870–881.